



**FACULTY  
OF MATHEMATICS  
AND PHYSICS**  
Charles University

**BACHELOR THESIS**

Martin Vavřík

**Simulation and Reconstruction  
of Charged Particle Trajectories  
in an Atypic Time Projection Chamber**

Institute of Particle and Nuclear Physics

Supervisor of the bachelor thesis: Mgr. Tomáš Sýkora, Ph.D.

Study programme: Physics

Prague 2025

9 I declare that I carried out this bachelor thesis independently, and only with the  
10 cited sources, literature and other professional sources. It has not been used to  
11 obtain another or the same degree.

12 I understand that my work relates to the rights and obligations under the Act  
13 No. 121/2000 Sb., the Copyright Act, as amended, in particular the fact that the  
14 Charles University has the right to conclude a license agreement on the use of this  
15 work as a school work pursuant to Section 60 subsection 1 of the Copyright Act.

In ..... date .....  
Author's signature



Title: Simulation and Reconstruction of Charged Particle Trajectories in an Atypical Time Projection Chamber Added hyphen to avoid overfull hbox

Author: Martin Vavřík

Institute: Institute of Particle and Nuclear Physics

Supervisor: Mgr. Tomáš Sýkora, Ph.D., Institute of Particle and Nuclear Physics

Abstract: Abstract.

Keywords: key words

# Contents

17		
18	<b>Motivation</b>	<b>2</b>
19	0.1 ATOMKI Anomaly . . . . .	2
20	0.1.1 ATOMKI Measurements . . . . .	2
21	0.1.2 Other Experiments . . . . .	3
22	0.2 X17 Project at IEAP CTU . . . . .	4
23	<b>1 Time Projection Chamber</b>	<b>7</b>
24	1.1 Orthogonal Fields TPC at IEAP CTU . . . . .	7
25	1.1.1 Coordinate Systems . . . . .	7
26	1.1.2 Magnetic Field Simulation . . . . .	8
27	<b>2 Track Simulation</b>	<b>11</b>
28	2.1 Microscopic Simulation . . . . .	11
29	2.2 Runge-Kutta Simulation . . . . .	12
30	<b>3 Track Reconstruction</b>	<b>13</b>
31	3.1 Reconstruction Assuming Steady Drift . . . . .	13
32	3.2 Ionization Electron Map . . . . .	15
33	3.2.1 Gradient Descent Search . . . . .	18
34	3.2.2 Interpolation on the Inverse Grid . . . . .	19
35	3.3 Discrete Reconstruction . . . . .	20
36	<b>4 Energy Reconstruction</b>	<b>22</b>
37	4.1 Cubic Spline Fit . . . . .	22
38	4.2 Circle and Lines Fit . . . . .	24
39	4.2.1 Two-dimensional fit . . . . .	24
40	4.2.2 Three-dimensional fit . . . . .	26
41	4.3 Runge-Kutta Fit . . . . .	26
42	<b>Conclusion</b>	<b>28</b>
43	<b>Bibliography</b>	<b>30</b>
44	<b>List of Figures</b>	<b>33</b>
45	<b>List of Tables</b>	<b>34</b>
46	<b>List of Abbreviations</b>	<b>35</b>

# Motivation

A Time Projection Chamber (TPC) is a type of gaseous detector that detects charged particle trajectories by measuring the positions and drift time of ions created in the gas; details are provided in Section 1. The energy of these particles can be inferred from the curvature of their trajectory in the magnetic field.

The goal of this thesis is to develop an algorithm for the reconstruction of charged particle trajectories and energy in an atypic TPC with orthogonal electric and magnetic fields, hereafter referred to as the Orthogonal Fields TPC (OFTPC), used in the X17 project at the Institute of Experimental and Applied Physics, Czech Technical University in Prague (IEAP CTU). Furthermore, we present the results of testing this algorithm with different samples of simulated data. (We use the Garfield++ toolkit [1] for simulations in combination with the ROOT framework [2] for data analysis and visualization. Some of our more demanding simulations are run on the MetaCentrum grid [3].)

The X17 project in IEAP CTU aims to reproduce measurements of anomalous behavior in the angular correlation distribution of pairs produced by the Internal Pair Creation (IPC) mechanism [4] during the decay of certain excited nuclei ( $^8\text{Be}$ ,  $^{12}\text{C}$ , and  $^4\text{He}$ ) observed by a team at ATOMKI in Hungary. **I would leave this here as a short summary before I explain it in more detail in the sections below.**

**Add citations: X17 project, VdG. Maybe also TPC, etc.**

## 0.1 ATOMKI Anomaly

Many theories propose the existence of new light bosons that are weakly coupled to ordinary matter [5]. These particles are potential dark matter candidates and could solve other issues with the Standard Model, such as the strong CP problem and the anomalous muon magnetic moment.

A possible way of detecting such bosons with a short lifetime is to observe nuclear transitions of excited nuclei. If a boson was emitted during the transition and subsequently decayed into an electron-positron pair, we could observe this as a peak on top of the  $e^+e^-$  angular correlation from IPC and External Pair Creation (EPC).

### 0.1.1 ATOMKI Measurements

Previously, there were several measurements of IPC in nuclear transitions in  $^8\text{Be}$  at Institute für Kernphysik (Frankfurt) [6, 7, 8] and at ATOMKI [9, 10] resulting in different anomalies with invariant mass in the range 5–15 MeV. This prompted a development of a better spectrometer.

In 2015, a group at ATOMKI led by Attila Krasznahorkay observed an anomalous IPC in  $^8\text{Be}$  [11]. They used the  $^7\text{Li}(p, \gamma)^8\text{Be}$  reaction at the  $E_p = 1030$  keV proton capture resonance to prepare the 18.15 MeV excited state ( $J^\pi = 1^+$ ,  $T = 0$ ). This state decays predominantly through M1 transitions to the ground state ( $J^\pi = 0^+$ ,  $T = 0$ ) and to the 3.03 MeV state ( $J^\pi = 2^+$ ,  $T = 0$ ) [12].

88 The angular correlation of the  $e^+e^-$  pairs created internally in these transitions  
 89 were measured and compared to the simulation; results from a narrow  $E_{\text{sum}} =$   
 90  $= 18$  MeV region are shown in Figure 1a. The simulation includes boson decay  
 91 pairs for different boson masses. The disparity parameter  $y$  is defined as

$$y = \frac{E_{e^-} - E_{e^+}}{E_{e^-} + E_{e^+}}, \quad (1)$$

92 where  $E_{e^-}$  and  $E_{e^+}$  are the kinetic energies of the electron and positron.

93 Their experimental setup was later upgraded ([details?](#)) and used for new mea-  
 94 surements. In 2022 the  $^8\text{Be}$  anomaly was also measured using the  $E_p = 441$  keV  
 95 resonance to produce the 17.64 MeV excited state ( $J^\pi = 1^+$ ,  $T = 1$ ) which again  
 96 decays primarily to the ground state and the 3.03 MeV state [12]. The anomaly  
 97 was also measured for  $E_p = 650$  and 800 keV where E1 transitions from the direct  
 98 proton capture dominate [13]. The results for  $e^+e^-$  with  $E_{\text{sum}} \in [13.5, 20]$  MeV  
 99 are shown in Figure 1b.

100 The newer setup was also used in 2021 to study the  $^3\text{H}(p, e^+e^-)^4\text{He}$  reaction at  
 101  $E_p = 510, 610$  and 900 keV [14], inducing direct and resonant capture populating  
 102 the overlapping first 20.21 MeV ( $J^\pi = 0^+$ ) and second 21.01 MeV ( $J^\pi = 0^-$ )  
 103 excited states [15]. The comparison of simulated and measured  $e^+e^-$  pair angular  
 104 correlations in the  $E_{\text{sum}} \in [18, 22]$  MeV region is shown in Figure 1c.

105 In 2022, another anomaly was measured in the  $^{11}\text{B}(p, e^+e^-)^{12}\text{C}$  process [16].  
 106 The  $E_p = 1388$  keV resonance was used to populate the 17.23 MeV excited state  
 107 ( $J^\pi = 1^-$ ,  $T = 1$ ) with a large width  $\Gamma = 1.15$  MeV [17]. This state decays  
 108 mainly through E1 transitions to the ground state  $J^\pi = 0^+$  and to the 4.44 MeV  
 109 state  $J^\pi = 2^+$ . To compensate for energy losses in the target, five energies in  
 110 the range  $E_p = 1.5$ – $2.5$  MeV were used. The experimental angular correlation for  
 111 the 17.23 MeV transition to the ground state is shown in Figure 1d.

112 Possible explanations of the anomaly include experimental effects, higher or-  
 113 der processes in the Standard Model [18, 19] or even a protophobic fifth force  
 114 mediated by a new 17 MeV boson X17 [20].

## 115 0.1.2 Other Experiments

116 Since the ATOMKI measurements, several experiments have been initiated to  
 117 attempt to replicate the results and search for the hypothetical X17 particle.

### 118 Two-arm $e^+e^-$ spectrometer in Hanoi

119 The anomaly in  $^8\text{Be}$  has been observed with  $> 4\sigma$  confidence by a team at the  
 120 Hanoi University of Sciences for  $E_p = 1225$  keV [21]. They built a two-arm  
 121 spectrometer in collaboration with ATOMKI and calibrated it using the 17.6 MeV  
 122 M1 transition. The results are shown in Figure 2.

### 123 Collisions at Nuclotron in Dubna

124 At the Joint Institute for Nuclear Research in Dubna, signal in the form of en-  
 125 hanced structures in the  $\gamma\gamma$  spectra at  $\sim 17$  and  $\sim 38$  MeV invariant masses  
 126 for  $p + \text{C}$ ,  $d + \text{C}$  and  $d + \text{Cu}$  reactions at momenta 5.5, 2.75, and 3.83 GeV per  
 127 nucleon [22]. Monte Carlo simulations support the conclusion that the signals  
 128 are a consequence of a decay of unknown particles X17 and E38.

## 129 The MEG II (Muon Electron Gamma) experiment

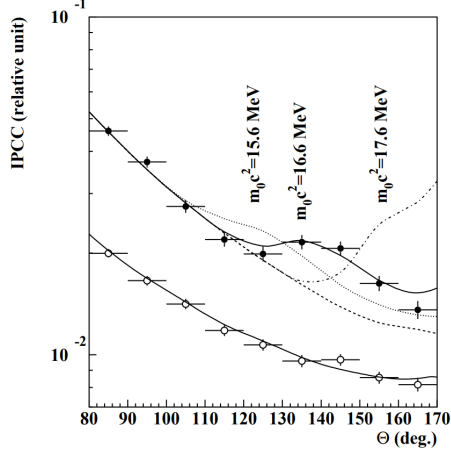
130 Experiments using the  ${}^7\text{Li}(p, e^+e^-){}^8\text{Be}$  reaction were carried out at the Paul  
131 Scherrer Institute with the MEG II superconducting solenoid spectrometer [23].  
132 Analysis of the data with  $E_p = 1080$  keV exciting both of the resonances (beam  
133 fully stopping in the target) found no significant evidence supporting the X17  
134 hypothesis. An upper bound (at 90% confidence) on the X17-to- $\gamma$  branching ra-  
135 tio was set at  $1.2 \cdot 10^{-5}$  for the 18.15 MeV state (larger than the ratio  $5.8 \cdot 10^{-6}$   
136 obtained by ATOMKI in 2016).

## 137 0.2 X17 Project at IEAP CTU

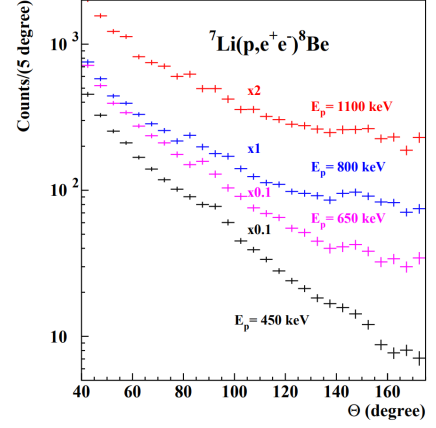
138 Short summary of our goals, maybe mention the grant.

- 139 •  ${}^7\text{Li}$  or  ${}^3\text{T}$  target, proton beam energies to be used to excite above mentioned  
140 states, energy range (detector should be able  $> 4$  MeV)
- 141 • three layers (TPX3, MWPC, TPC)
- 142 • multiple scattering problem (TPX3 in vacuum tube, carbon tube with  
143 thinned aluminum or Kapton windows, MWPC for exit point + trigger-  
144 ing/coincidence)
- 145 • TPC – energy, particle recognition (energy loss per unit distance), **more**  
146 **details in the next chapter**
- 147 • CAD drawing (with coordinate system defined in the next chapter, more  
148 figures will be there probably)
- 149 • TPX3 details: short description, maybe a mention of the tests
- 150 • couple of MWPC details could be above, TPC details in the next chapter

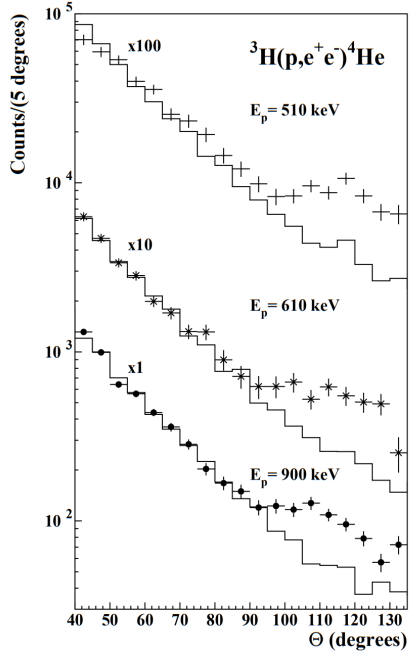




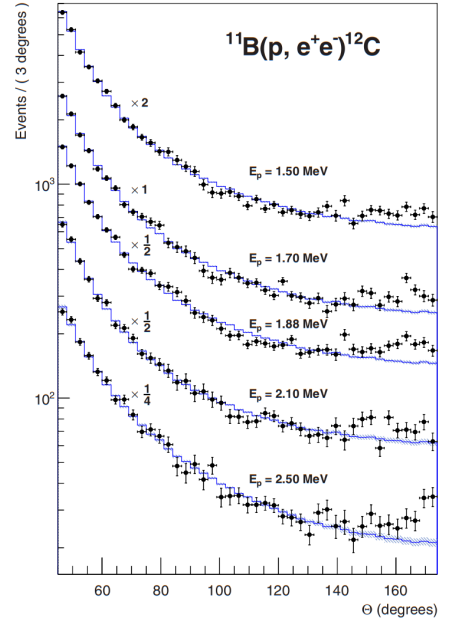
(a) Experimental  $e^+e^-$  pair correlations measured in the  ${}^7\text{Li}(p, e^+e^-){}^8\text{Be}$  reaction with  $|y| \leq 0.5$  (closed circles) and  $|y| \geq 0.5$  (open circles) [11].



(b) Experimental  $e^+e^-$  pair correlations measured in the  ${}^7\text{Li}(p, e^+e^-){}^8\text{Be}$  reaction with the improved setup for different proton beam energies [13].



(c) Experimental  $e^+e^-$  pair correlations measured in the  ${}^3\text{H}(p, e^+e^-){}^4\text{He}$  reaction with  $|y| \leq 0.3$  for different proton beam energies [14].



(d) Experimental  $e^+e^-$  pair correlations measured in the  ${}^{11}\text{B}(p, e^+e^-){}^{12}\text{C}$  reaction for different proton beam energies [16].

Figure 1: The ATOMKI anomalous IPC measured for different nuclei.

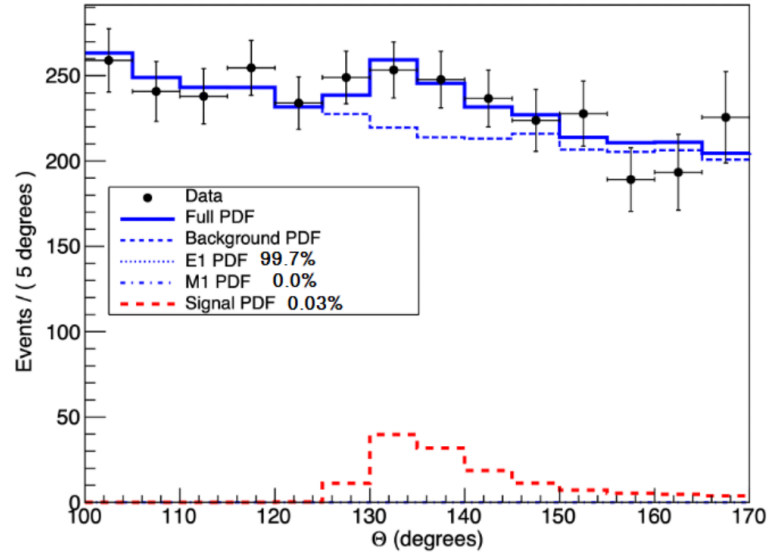


Figure 2: Results from the Hanoi spectrometer – angular  $e^+e^-$  pair correlations measured in the  ${}^7\text{Li}(p, e^+e^-){}^8\text{Be}$  reaction at  $E_p = 1225$  keV [21].

# 1. Time Projection Chamber

Description of TPC, working principle, standard vs. our field layout.

## 1.1 Orthogonal Fields TPC at IEAP CTU

Short description of our detector. Why we use an atypic TPC (benefits, complications). Gas mixture used in the detector (70/30) and its effect.

### 1.1.1 Coordinate Systems

In order to describe events in our detector, we use three distinct spaces: the detector space  $\mathcal{D}$ , the readout space  $\mathcal{R}$  and the pad space  $\mathcal{P}$ . Each space is later used to represent ionization electrons at different stages of the detection process: their creation in the gas, their final position when hitting the readout plane, and finally their representation in the discrete pad space.

#### Detector Space

The detector space  $\mathcal{D}$  represents the physical space of our detector. We describe it using Cartesian coordinates  $(x, y, z)$ . The  $z$ -axis is the detector's axis of symmetry, with its negative direction aligned with the proton beam. The origin  $(0, 0, 0)$  is located at the center of the irradiated target. The positive  $x$ -axis passes through the center of one of the OFTPCs along the intersection of its two planes of symmetry. The  $y$ -axis is then chosen to maintain a right-handed coordinate system.

Since the detector has a hexagonal symmetry, we use only one of its sectors in this work – the first sector  $\mathcal{D}_1 \subset \mathcal{D}$  which is defined by the condition:

$$(x, y, z) \in \mathcal{D}_1 \Leftrightarrow |y| \leq x \tan \frac{\pi}{6}. \quad (1.1)$$

Simulations in this sector can be applied to all sectors by rotating the coordinates accordingly. The volume of the OFTPC in this sector, which has the shape of a trapezoidal prism, has these boundaries:

$$x \in [x_{\min}, x_{\max}] = [6.51, 14.61] \text{ cm}, \quad (1.2)$$

$$z \in [z_{\min}, z_{\max}] = [-8, 8] \text{ cm}, \quad (1.3)$$

$$y_{\max}(x_{\min}) = -y_{\min}(x_{\min}) = 2.75 \text{ cm}, \quad (1.4)$$

$$y_{\max}(x_{\max}) = -y_{\min}(x_{\max}) = 7.45 \text{ cm}, \quad (1.5)$$

where  $y_{\max}(x)$  is the maximal value of the  $y$ -coordinate for a given  $x$ . The readout is located at  $z = 8 \text{ cm}$ ; for some purposes, we also define the distance to the readout  $d_r = 8 \text{ cm} - z$  as an alternative to the  $z$ -coordinate. Keeping this paragraph as it is because the OFTPC volume is distinct from the first sector and some parts of this thesis use the space beyond this volume.

## 180 Readout Space

181 The readout space  $\mathcal{R}$  represents the drift time and final positions of ionization  
 182 electrons as measured by an ideal continuous readout. We describe it using  
 183 coordinates  $(x', y', t)$ , where  $x'$  and  $y'$  correspond to the detector coordinates at  
 184 the readout plane ( $z = 8$  cm). **Currently not entirely sure how to put this into**  
 185 **a figure since only  $x'$  and  $y'$  correspond to the detector coordinates. The drift**  
 186 **time  $t$  is approximately proportional to  $d_r$ .**

## 187 Pad Space

188 The pad space  $\mathcal{P}$  represents the time bin and pad number of ionization electrons  
 189 as measured by an ideal discrete readout. **It is not really a subspace of  $\mathcal{R}$  but**  
 190 **there is a mapping from  $\mathcal{R}$  to  $\mathcal{P}$ . It is a discretization of a part of  $\mathcal{R}$ , the mapping**  
 191 **can be adjusted depending on the simulation. If we assume uniform electric field**  
 192 **there will be gaps, we don't use gaps in the reconstruction since the electrons**  
 193 **should be pulled towards the pads.**

194 The readout of the OFTPC will consist (**is the design final?**) of 128 rectangular  
 195 pads arranged in a staggered pattern (**add image where all the parameters are**  
 196 **marked**). Most of the pads are  $0.6 \times 0.9$  cm, only pads 102 and 124 are  $0.6 \times 0.6$  cm,  
 197 pad 127 is  $0.6 \times 0.509$  cm. The distance of neighboring pads is 0.08 cm, staggering  
 198 offset is 0.3946 cm.

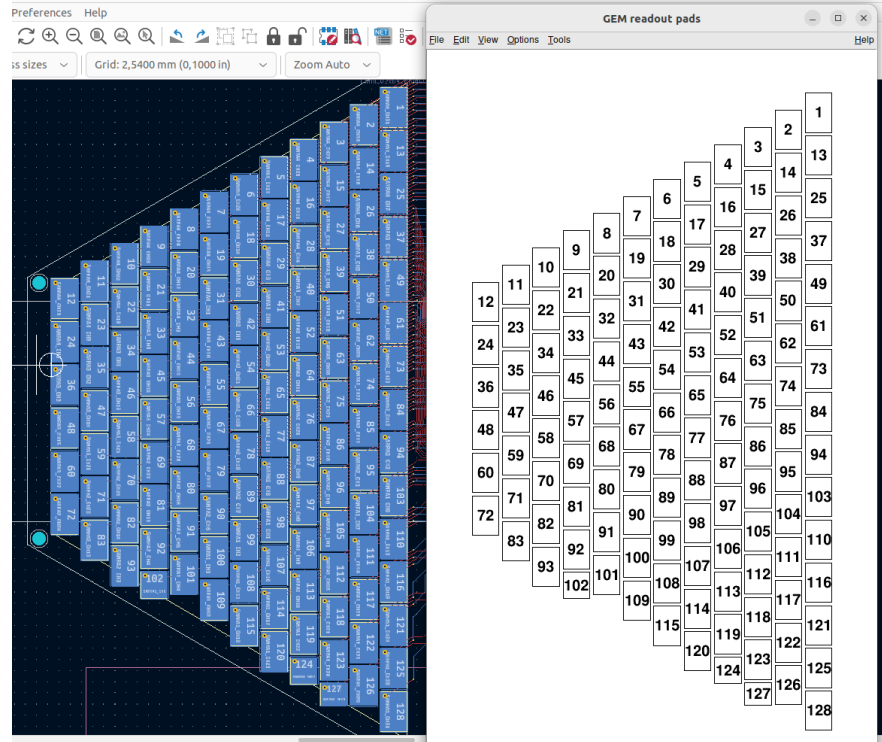


Figure 1.1: Pad layout of the TPC. **Swap for better image.**

### 199 1.1.2 Magnetic Field Simulation

200 **Magnetic field simulations in Maxwell (citation). Some figures. When working**  
 201 **with the magnetic field outside the regular grid, we use trilinear interpolation.**

## 202 Trilinear Interpolation

203 Trilinear interpolation is a 3D generalization of linear interpolation. It can be  
 204 used to interpolate a function whose values are known on a regular grid with  
 205 rectangular prism cells. We use this simple method for interpolating the magnetic  
 206 field, and it is later used in Section 3.2.1 to interpolate the Ionization Electron  
 207 Map, a key component of our track reconstruction algorithm. In both cases, we  
 208 use a regular cubic grid (apparently it is also called a Cartesian grid).

209 Could put a paragraph about linear interpolation here if it is not clear from  
 210 the equations below.

211 Let us consider a cell of our regular grid (a cube) with an edge of length  $a$   
 212 containing the point  $\mathbf{C} = (x, y, z)$  where we want to interpolate a function  
 213  $f: \mathbb{R}^3 \rightarrow \mathbb{R}$ . We know the values of this function at the vertices of the cell  
 214  $\mathbf{C}_{ijk} = (x_0 + ia, y_0 + ja, z_0 + ka)$ , where  $i, j, k \in \{0, 1\}$  are indices. We also define  
 215 the points  $\mathbf{C}_{ij} = (x, y_0 + ia, z_0 + ja)$  and  $\mathbf{C}_i = (x, y, z_0 + ia)$ . Then the interpolated  
 216 value  $\hat{f}(\mathbf{C})$  can be calculated as a composition of three linear interpolations (see  
 217 Figure 1.2):

$$\hat{f}(\mathbf{C}_{ij}) = (1 - x_d) f(\mathbf{C}_{0ij}) + x_d f(\mathbf{C}_{1ij}), \quad (1.6)$$

$$\hat{f}(\mathbf{C}_i) = (1 - y_d) \hat{f}(\mathbf{C}_{0i}) + y_d \hat{f}(\mathbf{C}_{1i}), \quad (1.7)$$

$$\hat{f}(\mathbf{C}) = (1 - z_d) \hat{f}(\mathbf{C}_0) + z_d \hat{f}(\mathbf{C}_1), \quad (1.8)$$

218 where  $x_d, y_d$ , and  $z_d$  are given as follows:

$$x_d = \frac{x - x_0}{a}, \quad y_d = \frac{y - y_0}{a}, \quad z_d = \frac{z - z_0}{a}. \quad (1.9)$$

219 We can also write

$$\hat{f}(\mathbf{C}) = \sum_{i,j,k \in \{0,1\}} t_x^i t_y^j t_z^k f(\mathbf{C}_{ijk}), \quad (1.10)$$

$$t_\alpha \stackrel{\text{def}}{=} \begin{pmatrix} t_\alpha^0 \\ t_\alpha^1 \end{pmatrix} = \begin{pmatrix} 1 - \alpha_d \\ \alpha_d \end{pmatrix}, \quad (1.11)$$

220 where  $\alpha \in \{x, y, z\}$  is an index. Furthermore, we can write  $\hat{f}(\mathbf{C})$  as a polynomial:

$$\hat{f}(\mathbf{C}) = \sum_{\alpha, \beta, \gamma \in \{0,1\}} \sum_{i=0}^{\alpha} \sum_{j=0}^{\beta} \sum_{k=0}^{\gamma} (-1)^{(\alpha-i)+(\beta-j)+(\gamma-k)} f(\mathbf{C}_{ijk}) x_d^\alpha y_d^\beta z_d^\gamma. \quad (1.12)$$

221 We take advantage of this form when generalizing trilinear interpolation to irreg-  
 222 ular grid in section 3.2.2.

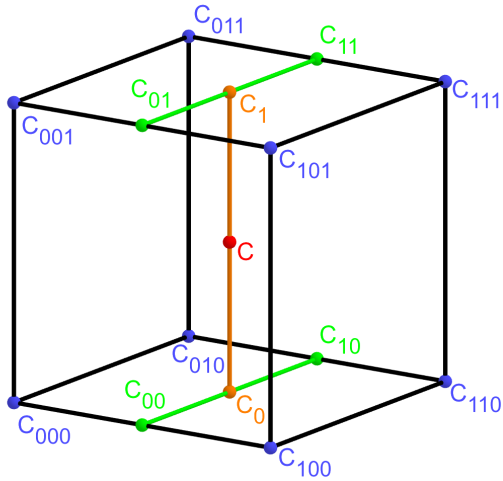


Figure 1.2: Visualization of trilinear interpolation as a composition of linear interpolations. Image drawn in GeoGebra and inspired by a similar image on Wikipedia (which looks a bit worse) – is credit necessary?

223 Maybe a citation here, although I am not sure it is necessary since it could  
 224 be considered common knowledge. The last two equations are my own. Maybe  
 225  $x_0$ , etc. should be explicitly described.

## 2. Track Simulation

In order to develop and test the reconstruction algorithm, electron and positron tracks are simulated inside the first sector  $\mathcal{D}_1$  of our detector (see Section 1.1.1) with different initial parameters. Two approaches are currently used to simulate tracks, each of them for different purpose.

The **Microscopic Simulation** uses the Garfield++ toolkit [1]. Within this toolkit, the High Energy Electro-Dynamics (HEED) program [24] is used to simulate the primary particle and the class *AvalancheMicroscopic* to simulate the drift of secondary electrons created by ionization in the gas. This is the most precise and time-consuming simulation used; our current goal is to be able to successfully reconstruct its results and determine our best-case energy resolution.

The **Runge-Kutta Simulation** uses the 4th order Runge-Kutta numerical integration (add citation for Runge-Kutta) to simulate the trajectory of the primary particle in the electromagnetic field inside the detector. It is relatively fast since it does not simulate the secondary particles. It is used as part of our reconstruction algorithm and for testing some parts of the reconstruction.

All of these simulations require the knowledge of the electromagnetic field inside the detector. A uniform electric field of  $400 \text{ V}\cdot\text{cm}^{-1}$  is assumed. The magnetic field was simulated in Maxwell (see Section 1.1.2). add citation

Single track in positive x direction or initial parameter randomization. Importance of gas composition, used gas compositions.

### 2.1 Microscopic Simulation

The microscopic simulation, the most detailed simulation used in this work, is performed using the Garfield++ toolkit [1].

The electron transport properties are simulated using the program Magboltz (Add citation.). Two different gas mixtures were used: 90% Ar + 10% CO<sub>2</sub> and 70% Ar + 30% CO<sub>2</sub>. The second mixture will be used in our detector. The temperature is set to 20 °C, the pressure is atmospheric.

The primary track is simulated using the program HEED [24], which is an implementation of the photo-absorption ionization model. This program provides the parameters of ionizing collisions. HEED can also be used to simulate the transport of delta electrons; we do not account for these in the current simulation but plan to include them in the future. The photons created in the atomic relaxation cascade (fluorescence reabsorption, ?) are also not simulated.

Finally, we use the microscopic tracking provided by the class *AvalancheMicroscopic* to simulate the drift of the ionization electrons. Each electron is followed from collision to collision using the equation of motion and the collision rates calculated by Magboltz.

First simulated track in the z direction should be described in detail here (own subsection?). Figures.

Add more detailed and better description of HEED, and microscopic tracking (each their own subsection?). Could also mention Monte Carlo (requires gas file generation) and Runge-Kutta simulation implemented in Garfield, why we don't

269 use them (another subsection? rename the section to Garfield++ simulation and  
 270 mention all relevant parts?).

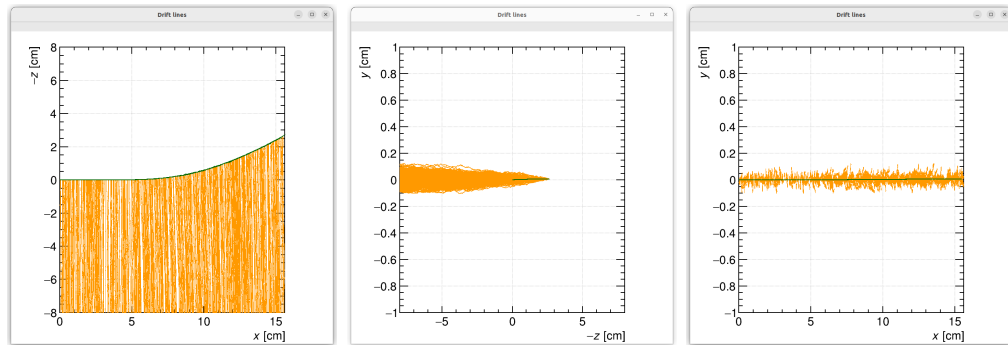


Figure 2.1: Example of a simulated electron track in 70 % argon and 30 % CO<sub>2</sub> atmosphere (on the left). Swap for better images, better zoom. Explain drift lines, primary particle.

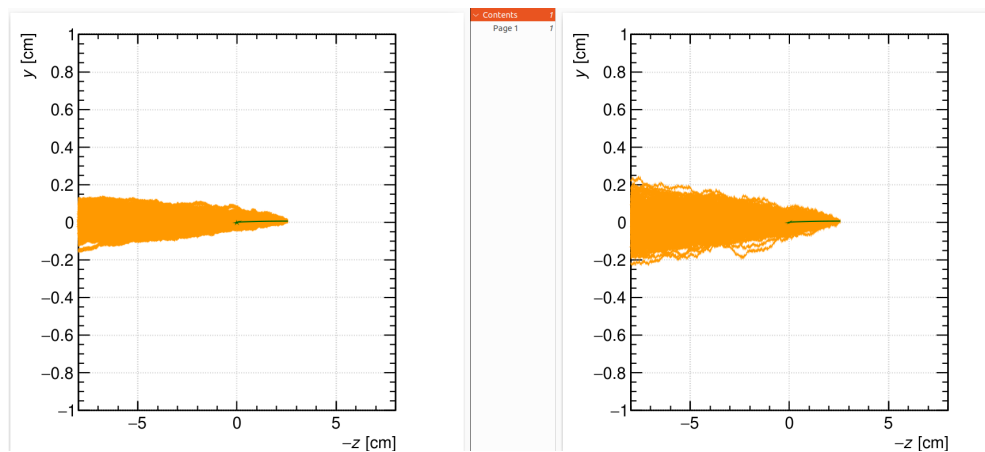


Figure 2.2: Comparison of diffusion in a simulated electron track in 70 % argon, 30 % CO<sub>2</sub> atmosphere and in 90 % argon, 10 % CO<sub>2</sub> atmosphere (on the right). Swap for better image, better zoom. Or put the same pictures for both comparisons in one subfigure, etc. Describe better.

## 271 2.2 Runge-Kutta Simulation

272 Trajectory simulation with 4th order Runge-Kutta. Relativistic equation that is  
 273 numerically integrated by the algorithm.



### 3. Track Reconstruction

In the first stage of the reconstruction algorithm, we reconstruct the track of a primary particle (either an electron or a positron). The result of this step is then used to determine the energy of the particle (Section 4).

The **Reconstruction Assuming Steady Drift** uses the standard TPC approach. With parallel fields, the drift inside a uniform electric field remains undistorted (reference to some future part of the TPC chapter). Therefore, we only need to reconstruct the  $z$ -coordinate from the drift time using the known drift velocity. We also assume that the readout coordinates  $(x', y', t)$  are known exactly, neglecting the pads and time bins.

Reconstruction using the **Ionization Electron Map** (from now on referred to as *the map*) uses a simulation of the drift of secondary (ionization) electrons within the detector volume. This simulation can then be used to interpolate the initial position of the secondary electrons. First attempts neglect the pads.

We use the map for reconstruction in two different ways. The first one uses gradient descent search along with trilinear interpolation (see Section 1.1.2) of the map. The second method uses interpolation on the irregular inverse grid with a linear polynomial.

The **Discrete Reconstruction** uses the map; instead of reconstructing the exact position of each electron, we reconstruct the center of each hit pad with the time corresponding to the midpoint of the time bin. The electron count in each TPC bin (consisting of the pad and the time bin) serves as the charge value, which is then used as a weight in the energy reconstruction fit.

#### 3.1 Reconstruction Assuming Steady Drift

As the first step, we decided to try to reconstruct an electron track with a special set of initial parameters. The origin of the particle is given by the origin of our coordinate system. The initial direction is given by the positive  $x$ -axis. This means the magnetic field of our detector is perpendicular to the momentum of the particle at all times, and we can reduce the problem to two-dimensional space. As an example, we use a track simulated using the microscopic simulation (see Section 2.1) with a kinetic energy of 8 MeV. The gas composition used in this simulation is 90% Ar + 10% CO<sub>2</sub>. Might be better to describe this track in Section 2.1.

In this approach to the reconstruction of the track, we decided to use the common method used in a standard TPC. This will allow us to explore the significance of the atypical behavior in our OFTPC. Additionally, we assume the readout is continuous to further simplify the problem. In this approximation, we reconstruct the initial position of each ionization electron.

The reconstruction is then defined by the following relations between the coordinates of the detector space and the readout space (see Section 1.1.1):

$$x = x', \tag{3.1}$$

$$y = y', \tag{3.2}$$

$$z = v_d t, \tag{3.3}$$

314 where  $v_d$  is the drift velocity of electrons in the given gas mixture. At a phe-  
 315 nomenological level, this velocity can be considered as a function of the electric  
 316 field  $\mathbf{E}$  and the magnetic field  $\mathbf{B}$ :

$$v_d = v_d(\mathbf{E}, \mathbf{B}). \quad (3.4)$$

317 Equation taken from Garfield user manual. The Garfield++ toolkit uses this  
 318 fact to accelerate their drift simulation with non-microscopic approaches (could  
 319 mention in the simulation chapter). Since we assume a uniform electric field in  
 320 our detector and we want to neglect the effect of our unusual magnetic field, we  
 321 consider the drift velocity to be constant in this scenario. We then approximate  
 322 this velocity by fitting the dependence  $z(t)$  taken from the simulated ionization  
 323 electrons. This is in one of the provisional figures. Also, this description is  
 324 not completely accurate; in reality, we fit  $t1:8-y0$  with  $a1*x+a0$  and then invert  
 325 this and use  $8-y0 = b1*t1+b0$  (old coordinates);  $b1=1/a1$  functions as the drift  
 326 velocity. Maybe also define this 8-z variable as an alternative to  $z$  in Section 1.1.1  
 327 and then use it when correcting this.

328 Later, in a commit after this, I plotted some residues (provisional figure),  
 329 which could be useful, but for some reason they are residuals from a spline fit of  
 330 the track?! Probably redo this without the spline fit; just explore the difference  
 331 in individual points.

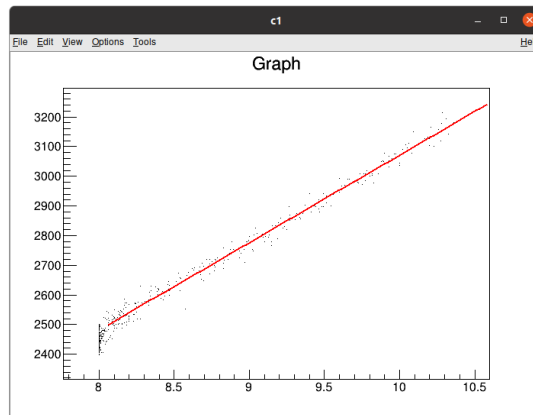


Figure 3.1: Dependence of the drift time on the  $z$  coordinate in 90 % argon and 10 %  $\text{CO}_2$  atmosphere, fitted with a linear function. The fitted function gives us the average drift velocity in the gas and can be used for rough reconstruction in our TPC. Swap for better image with axis labels, etc. Maybe write the fitted equation.

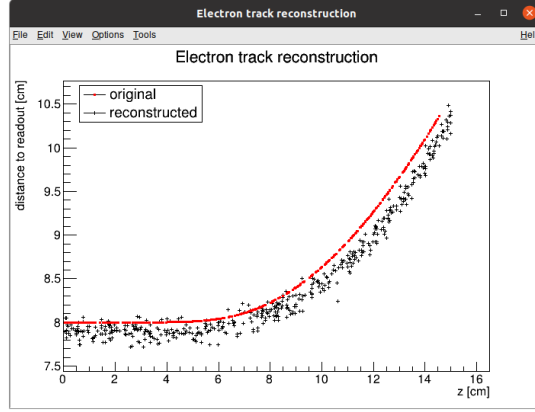


Figure 3.2: First attempt at a track reconstruction using only the drift velocity. This approach works well in a standard TPC (ideally cite some source?). 90 % argon and 10 % CO<sub>2</sub> atmosphere. Swap for better image, correct coordinates.

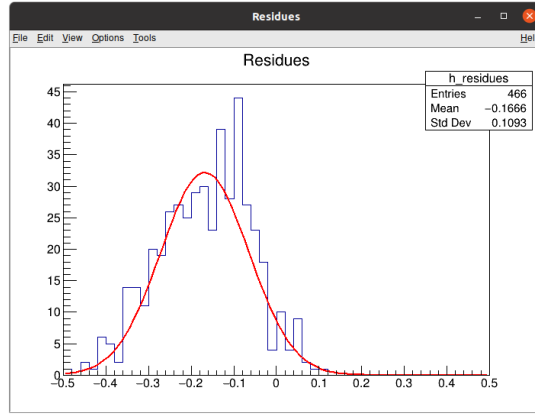


Figure 3.3: First attempt at a track reconstruction using only the drift velocity, residues. Swap for better image, correct coordinates. What's causing the shift? Explain details.

## 3.2 Ionization Electron Map

Inside an OFTPC, the drift of the secondary (ionization) electrons is significantly affected by its magnetic field (pictures of the distortion later, the effect is bigger for the 90/10 composition.). We need to take this into account for accurate reconstruction. In the first approximation, we assume a continuous readout (i.e., we neglect pads). We can then reconstruct the original position of each ionization electron using its readout coordinates. For this purpose, we use the ionization electron map.

The ionization electron map represents a mapping from the detector space to the readout space (see Section 1.1.1). It tells us what readout coordinates  $(x', y', t)$  we can expect on average for an ionization electron created at the detector coordinates  $(x, y, z)$ . More precisely it is a mapping to the distributions on the readout space; we can simplify this as only the means  $\bar{\mathcal{M}}$  and the covariance

345 matrices  $\mathcal{M}_{\text{cov}}$ , assuming Gaussian distribution.

$$\mathcal{M} : \mathcal{D} \longrightarrow \mathcal{R}, (x, y, z) \longmapsto (x', y', t). \quad (3.5)$$

346 To get an approximation of this mapping, we simulate the drift of ionization  
 347 electrons generated on a regular grid inside the volume of our OFTPC <sup>1</sup>. It  
 348 is also useful to simulate multiple (100 in our case) electrons originating from  
 349 the same position so we can get a better information about the average drift  
 350 and its variance. In order to get more accurate results, we use the microscopic  
 351 simulation of these electrons described in Section 2.1. When evaluating the map  
 352 inside the grid, we use trilinear interpolation (see Section 1.1.2). From now on,  
 353 we will denote this interpolated simulation with the same symbol  $\mathcal{M}$ .

354 Finally, we need to invert the map to get the original detector coordinates  
 355  $(x, y, z)$  for the given readout coordinates  $(x', y', t)$ . In our case, we can reason-  
 356 ably assume that the mapping  $\overline{\mathcal{M}}$  is one-to-one (as seen in the simulations). We  
 357 implemented two methods for this purpose: the gradient descent search (Sec-  
 358 tion 3.2.1) and interpolation on the inverse grid (Section 3.2.2).

359 The simulation of the map is a computationally heavy task. For this reason,  
 360 we use the MetaCentrum grid [3] to parallelize needed calculations. At first, this  
 361 was done by evenly distributing the simulated electrons across the individual jobs  
 362 in a simulation with only one electron per vertex in the regular grid with a spacing  
 363 of one centimeter.

364 Later, a more efficient approach was implemented, accounting for the varying  
 365 lengths of the drift of individual electrons. If we index the electrons in the order  
 366 of increasing coordinates  $y, x, z$  (picture?), we can express the number  $n_l$  of full  
 367 XY layers (i.e., electrons with the same  $z$  coordinate) of electrons with index less  
 368 than or equal to  $i$

$$n_l(i) = \left\lfloor \frac{i}{n_{xy}} \right\rfloor, \quad (3.6)$$

369 where  $n_{xy}$  is the number of electrons in each XY layer calculated simply by count-  
 370 ing the electrons that satisfy boundary conditions for  $x$  and  $y$ . These conditions  
 371 should be mentioned above; sector condition + maximal  $x$  value. The number of  
 372 electrons remaining in the top layer is then

$$n_r(i) = i \bmod n_{xy}. \quad (3.7)$$

373 Finally, we can calculate the sum of the drift gaps of electrons up to index  $i$

$$d_{\text{sum}} = (z_{\text{max}} - z_{\text{min}})n_{xy}n_l - \frac{n_l(n_l - 1)}{2}n_{xy}l + n_r(z_{\text{max}} - z_{\text{min}} - n_l l). \quad (3.8)$$

374 We then use a binary search algorithm to find the maximum index  $i$  such that  
 375 the value of this sum is less than the fraction  $\frac{\text{job id}}{\text{max job id}}$  of the total sum. This way  
 376 we obtain the minimal and the maximal index of electrons simulated in the given  
 377 job. The spacing  $l$  should be probably defined above + picture of the simulating  
 378 grid (1 layer). zmin zmax also

379 After the simulation of the map, we calculate the mean readout coordinates  
 380 assuming Gaussian distribution (i.e., we use averages). We also calculate standard

---

<sup>1</sup>we do not take the detector walls into account and simulate even outside of the OFTPC which lets us interpolate even close to the walls

381 deviations in a later commit, should be upgraded to the covariance matrix. We  
 382 never actually plotted the distributions we get when simulating the same electron  
 383 multiple times, so we do not know if our assumptions are accurate (could also  
 384 run some statistical test to see how well the Gaussian distribution fits).

385 The obtained map is then stored in a custom class template *Field*, could  
 386 expand on that. Maybe earlier, since the same template is used for the magnetic  
 387 field.

388 Could insert a table here describing all 4 simulations of the map (gas composi-  
 389 tion, spacing, etc.). Simulation inside of one sector (at first double angle). Extra  
 390 space on the sensor. Edge cases not taken into account (TPC wall). Using qsub  
 391 (not sure if important). Add plots of distortion of the coordinates. Could also do  
 392 these plots in a different way (e.g., drawing all the endpoints of each ionization  
 393 electron or some error ellipse plot).

394 Images to add (comparison of both simulations):

- 395 • 3D visualization of the map, simulation example
- 396 •  $z$  vs.  $t$  plot
- 397 • XY plane distortion for different  $z$  values; with arrows and error bars, for  
 398 all  $z$ -layers with different colors
- 399 • XZ plane ( $y = 0$ ) distortion in  $x$  (maybe not necessary?)
- 400 • XT plot ( $y = 0$ ) showing (small) distortion in drift times

401 More images:

- 402 • Residuals of the continuous readout reconstruction.

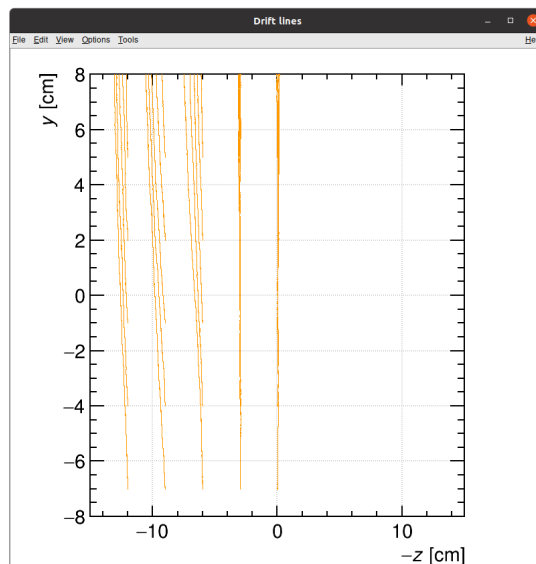


Figure 3.4: Example of map generation. Swap for better image, correct coordinates.

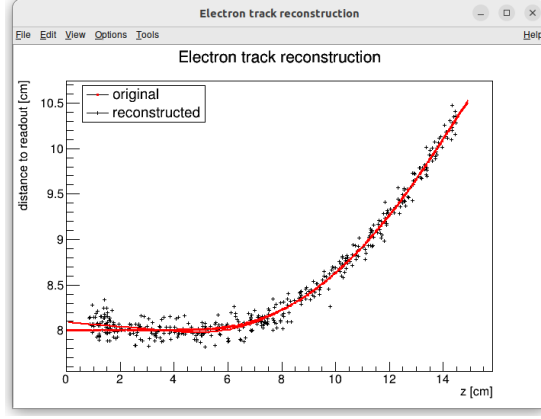


Figure 3.5: Example reconstruction with the map. Swap for better image, correct coordinates.

### 3.2.1 Gradient Descent Search

The first implemented method of reconstruction uses a gradient descent search to calculate an inversion of the map  $\bar{\mathcal{M}}$  in a given point. Gradient descent is an iterative minimization algorithm for multivariate functions. Let  $R \in \mathcal{R}$  be a point in the readout space; we want to find a point  $D = (x, y, z) \in \mathcal{D}$  in the detector space such that

$$\bar{\mathcal{M}}(D) = R = (x'_R, y'_R, t_R). \quad (3.9)$$

We define a function  $f_R$  in the readout space as a distance in this space:

$$f_R(x', y', t) = \sqrt{(x' - x'_R)^2 + (y' - y'_R)^2 + v_d^2(t - t_R)^2}, \quad (3.10)$$

where  $v_d$  is an approximation of the drift velocity in the TPC, obtained from the reconstruction in Section 3.1 (there will be an image with the linear fit there). We make an initial guess (actually in the original code we just take  $z = 0$ ):

$$D_0 = (x'_R, y'_R, v_d t). \quad (3.11)$$

Assuming we have the  $n$ -th estimate  $D_n$ , we calculate the  $i$ -th component of the gradient of  $f_R \circ \bar{\mathcal{M}}$  numerically using central differences:

$$\left[ \nabla(f_R \circ \bar{\mathcal{M}}) \right]^i(D_n) \approx \frac{f_R(\bar{\mathcal{M}}(D_n + s \cdot e^i)) - f_R(\bar{\mathcal{M}}(D_n - s \cdot e^i))}{2s}, \quad (3.12)$$

where  $e^i \in \mathcal{D}$  is the  $i$ -th coordinate vector and  $s$  is the step size. The step size should be sufficiently small; initially, we set it as a fraction of the map's grid spacing  $s = \frac{l}{10}$ . During the minimization, we check that  $f_R(\bar{\mathcal{M}}(D_n)) < 10s$  at all times. When using trilinear interpolation, it would be more efficient to calculate the gradient explicitly ( $\pm$  same result). This could be implemented inside the *Field* template class. The next iteration can be calculated as follows:

$$D_{n+1} = D_n - \gamma \nabla(f_R \circ \bar{\mathcal{M}})(D_n), \quad (3.13)$$

where  $\gamma \in \mathbb{R}^+$  is the damping coefficient. It should be set to a small enough value to ensure convergence, but large enough for sufficient converging speed.

423 The minimization stops either when the error  $f_R(\overline{\mathcal{M}}(D_n))$  drops below a specified  
 424 value or when the number of iterations exceeds a certain limit (in this case,  
 425 a message is printed into the console). The parameters of this method can be  
 426 further optimized (e.g., a better choice of  $\gamma$ , **gradient computation**); instead, we  
 427 later decided to use the interpolation on the inverse grid described in the next  
 428 section.

429 **Measure reconstruction duration and compare it with the inverse grid inter-**  
 430 **polation? Also compare the result? Not sure if this has to be cited.**

### 431 3.2.2 Interpolation on the Inverse Grid

432 **Interpolating between known points in the readout space. Gaussian elimina-**  
 433 **tion, multivariate polynomial. Benefits compared to the gradient descent search**  
 434 **method (one-time computation for the whole map is easy to achieve if needed).**

435 The currently used baseline reconstruction method is the interpolation on  
 436 the inverse grid. Rather than attempting to invert the trilinearly interpolated  
 437 map as in the previous section, we take advantage of the fact that the map  $\overline{\mathcal{M}}$   
 438 is one-to-one (**isomorphism is supposed to preserve structure, not sure how to**  
 439 **interpret that here**). Since we have simulated values of this map on a regular  
 440 grid in the detector space  $\mathcal{D}$ , we also know the inverse map  $\overline{\mathcal{M}}^{-1}$  on the irregular  
 441 inverse grid in the readout space  $\mathcal{R}$ . To get an approximation of the inverse map  
 442 in the entire readout space, we can use interpolation.

443 Since the inverse grid is irregular, trilinear interpolation cannot be applied.  
 444 Given that the simulated map is dense enough to provide a good approxima-  
 445 tion considering the size of our pads, we can adopt a similar approach (more  
 446 complicated and computationally heavy alternative would be natural neighbor  
 447 interpolation). As shown in Equation 1.12 in Section 1.1.2, trilinear interpolation  
 448 can be expressed as a polynomial:

$$\hat{f}(x, y, z) = axyz + bxy + cxz + dyz + ex + fy + gz + h, \quad (3.14)$$

449 where  $a, b, c, d, e, f, g, h$  are coefficients uniquely determined by the values of  
 450 the function at the vertices of the interpolation cell. We can generalize this  
 451 for a function defined on an irregular grid. Given the function values at any eight  
 452 points, we can write a system of eight linear equations

$$\begin{pmatrix} x_1 y_1 z_1 & x_1 y_1 & x_1 z_1 & y_1 z_1 & x_1 & y_1 & z_1 & 1 \\ \vdots & \vdots & \vdots & \vdots & \vdots & \vdots & \vdots & \vdots \\ x_8 y_8 z_8 & x_8 y_8 & x_8 z_8 & y_8 z_8 & x_8 & y_8 & z_8 & 1 \end{pmatrix} \begin{pmatrix} a \\ \vdots \\ h \end{pmatrix} = \begin{pmatrix} f(x_1, y_1, z_1) \\ \vdots \\ f(x_8, y_8, z_8) \end{pmatrix}, \quad (3.15)$$

453 which has a unique solution for the coefficients for most values of  $(x_n, y_n, z_n)$  and  
 454  $f(x_n, y_n, z_n)$ , where  $n \in \{1, \dots, 8\}$ .

455 This approach introduces a small complication: finding the correct pseudo-  
 456 cell (i.e., the image of eight vertices forming a cubic cell in the regular grid) in  
 457 the inverse grid. The eight irregularly spaced vertices of this pseudocell do not  
 458 define a unique volume, so there are multiple possible ways to partition  $\mathcal{R}$  into  
 459 pseudocells, with no obvious choice among them.

460 **We are currently ignoring this problem and performing binary search along**  
 461  **$x, y, z$  (in this order). It shouldn't matter too much because the 70/30 map**



462 doesn't cause such a big distortion and was even accidentally extrapolated for all  
 463  $z$  different from the central plane. Interpolation should be generally faster than  
 464 the gradient descent since we don't need to iterate. We also don't need to optimize  
 465 it to improve performance, if it's too slow we can even calculate the coefficients  
 466 for the entire map before reconstruction.

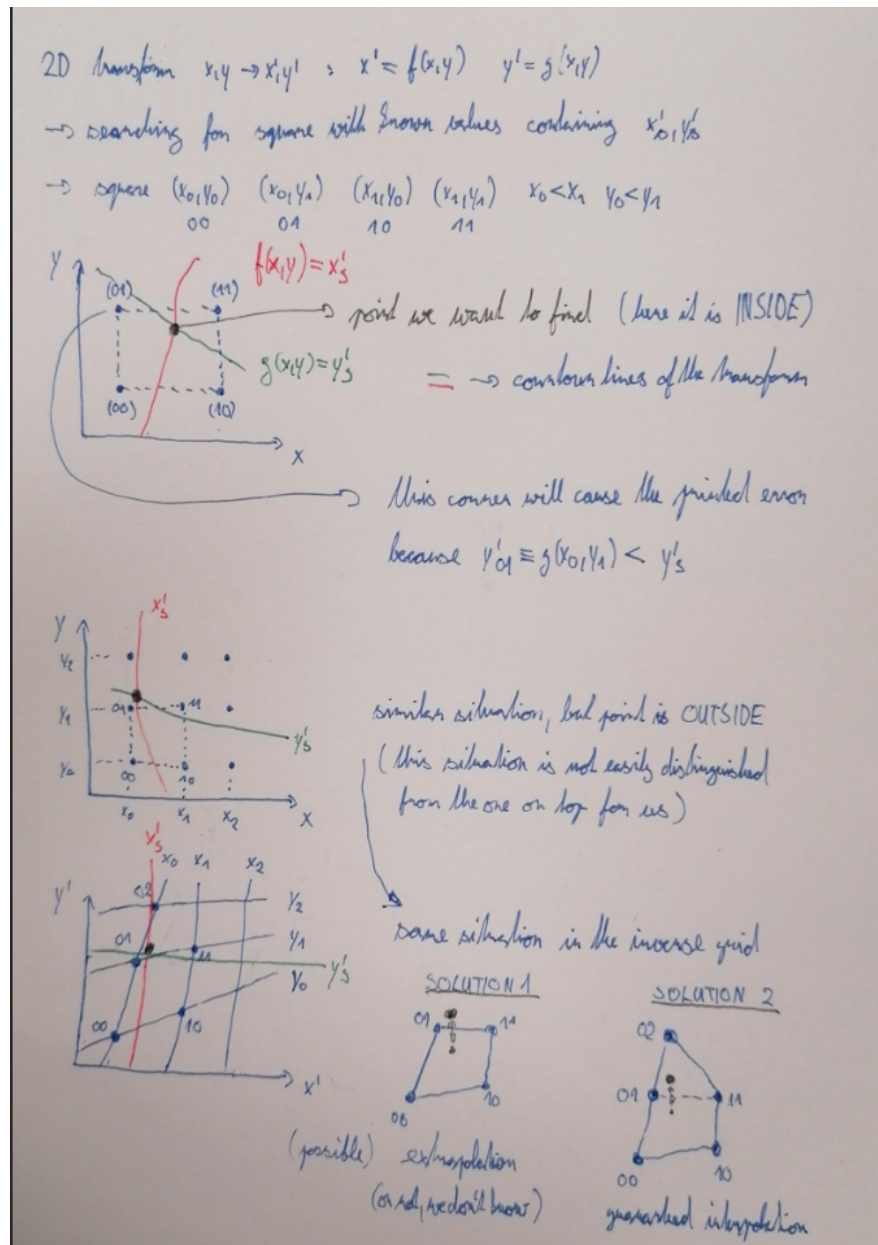


Figure 3.6: Selection of the points for interpolation. Create better images; use the explanation interpolation vs. extrapolation strange property. Solution 2 probably does not make much sense.

### 467 3.3 Discrete Reconstruction

468 Reconstruction with pads and time bins. Maybe testing different pads. Mapping  
 469 the center of the pad (along with the midpoint of the time bin) isn't necessarily



470 the best approach since it might not correspond to the average parameters of  
471 an electron with these readout parameters (insignificant?).

472 It is also possible to make this a subsection of the map, making the previous  
473 subsections parts of a new subsection 'Map Inversion'.

## 4. Energy Reconstruction

The second stage is the reconstruction of the particle's energy using a fit of its reconstructed track (see Section 3). We have tested three ways of reconstructing the energy. Fitting is done using the MINUIT algorithm implemented in ROOT [2]. [Cite some CERN article directly on MINUIT, can add a section.](#)

The **Cubic Spline Fit** is a tested and later rejected method of energy reconstruction. It uses smoothly connected piecewise cubic polynomials between uniformly spaced nodes. Energy is calculated using the fit parameters by computing the radius of curvature in different points of the fitted curve using the known magnitude of the magnetic field perpendicular to the trajectory. We rejected this method because tuning of the fit to have a reasonably stable radius of curvature turned out to be unpractical.

The **Circle and Lines Fit** was chosen as an alternative since this corresponds to the shape of a trajectory of a charged particle crossing a finite volume with a homogeneous magnetic field. The energy of the particle can be estimated using the fitted radius and the magnitude of the perpendicular magnetic field in the middle of the TPC.

The **Runge-Kutta Fit** uses the 4th order Runge-Kutta numerical integration described in Section 2.2. Initial parameters of the track (including the particle's energy) are optimized so that the integrated trajectory fits to the reconstructed one. This fit can also be performed as a single parameter (i.e., energy) fit if we get the initial position and orientation of the particle on the entrance to the TPC from previous detectors (Timepix 3 (Tpx3) and Multi-Wire Proportional Chamber (MWPC), see Section 0.2).

### 4.1 Cubic Spline Fit

The first attempt to get an early estimate of the kinetic energy of the particle uses a cubic spline fit. We use an electron track starting in the origin of our coordinate system with an initial direction in the positive  $x$  axis. The example track is simulated microscopically (see Section 2.1) with a kinetic energy of 8 MeV in a gas mixture 90% Ar + 10% CO<sub>2</sub> (the same track was used in Section 3.1).

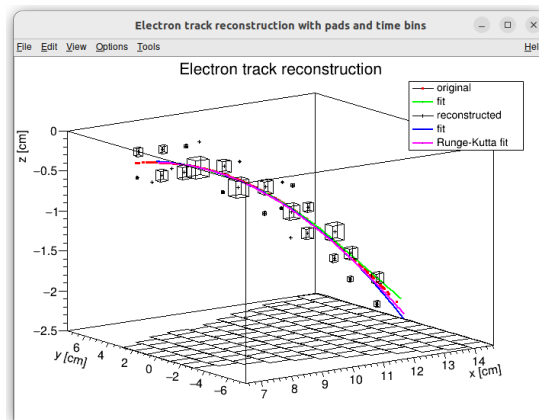


Figure 4.1: Example of a fitted reconstructed track. [Swap for better image.](#)

504 This track should probably be described in the simulation chapter.

505 In order to calculate the spline, we use the class *TSpline3* from ROOT. This  
 506 allows us to evaluate the spline using the coordinates  $(x_n, z_n)$  of each node and  
 507 the derivatives  $d_1, d_2$  in the first and the last node. We can fit these parameters  
 508 of a fixed amount of nodes to the simulated trajectory. We use the IMPROVE  
 509 algorithm provided by the *TMinuit* class in ROOT. This algorithm attempts to  
 510 find a better local minimum after converging.

511 After the fit, we want to get an energy estimate. In order to calculate it, we  
 512 need the radius of curvature, which we get from the fitted spline at every point  
 513 of the trajectory. The part of the spline corresponding to a given node is defined  
 514 as

$$z(x) = z_n + b\Delta x + c(\Delta x)^2 + d(\Delta x)^3, \quad (4.1)$$

515 where  $\Delta x = x - x_n$  and  $b, c, d$  are coefficients. Using this equation, we derive  
 516 the radius of curvature<sup>1</sup> as:

$$r(x) = \frac{(1 + z'^2(x))^{\frac{3}{2}}}{z''(x)} = \frac{(1 + (b + 2c\Delta x + 3d(\Delta x)^2)^2)^{\frac{3}{2}}}{2c + 6d\Delta x}. \quad (4.2)$$

517 Based on the geometry of the detector, we can assume the magnetic field  
 518  $\mathbf{B}(x, 0, z) = (0, B(x, z), 0)$  for a track in the XZ plane. Since the electron is rela-  
 519 tivistic, the effect of the electric field on its trajectory is negligible. The Lorentz  
 520 force  $F_L$  is then always perpendicular to the momentum of the electron and acts  
 521 as a centripetal force  $F_c$ :

$$\mathbf{F}_L = \mathbf{F}_c, \quad (4.3)$$

$$\|e\mathbf{v} \times \mathbf{B}\| = \frac{\gamma m_e v^2}{r}, \quad (4.4)$$

$$ec\beta B = \frac{E_{0e}\beta^2}{r\sqrt{1 - \beta^2}}, \quad (4.5)$$

$$\sqrt{1 - \beta^2} = \frac{E_{0e}\beta}{ecBr}, \quad (4.6)$$

522

$$\beta^2(x) = \left[ 1 + \left( \frac{E_{0e}}{ecB(x, z(x))r(x)} \right)^2 \right]^{-1}, \quad (4.7)$$

523 where  $e$  is the elementary charge,  $c$  is the speed of light in vacuum,  $m_e$  is the rest  
 524 mass of electron,  $E_{0e} = m_e c^2$  is the corresponding energy,  $\gamma$  is the Lorentz factor,  
 525  $\mathbf{v}$  is the velocity of the electron, and  $\beta = \frac{v}{c}$ . We can then finally get our estimate  
 526 of the kinetic energy for a given point on the trajectory as follows:

$$E_{\text{kin}}(x) = \left( \frac{1}{\sqrt{1 - \beta^2(x)}} - 1 \right) E_{0e}. \quad (4.8)$$

527 We can then average these estimates at multiple points to get one final estimate.  
 528 This method was later rejected in favor of the circle and lines fit described in  
 529 Section 4.2. Add some figures.

---

<sup>1</sup>For the general formula see [https://en.wikipedia.org/wiki/Curvature#Graph\\_of\\_a\\_function](https://en.wikipedia.org/wiki/Curvature#Graph_of_a_function)

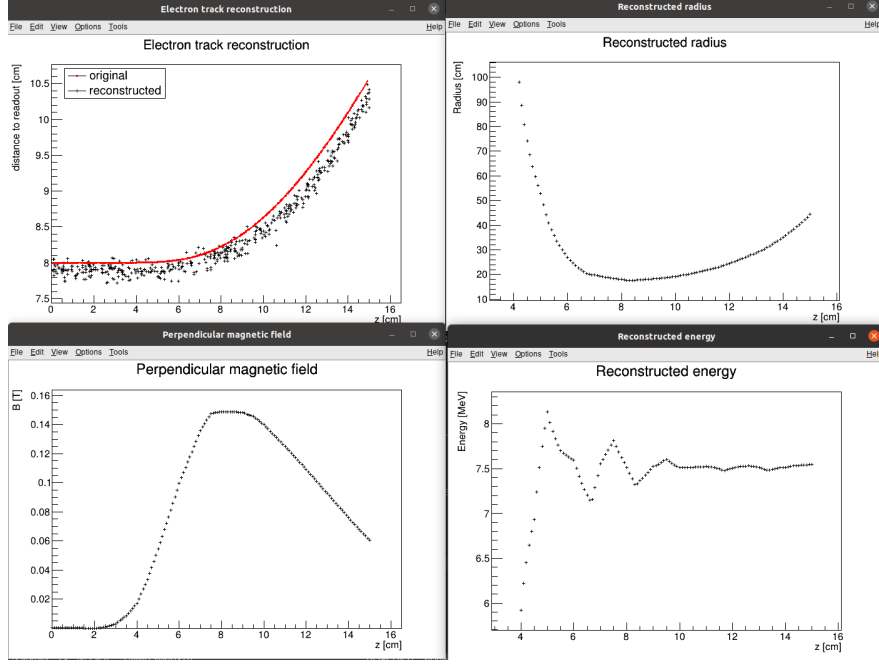


Figure 4.2: First attempt at a track reconstruction using only the drift velocity. Spline energy reconstruction attempt. **Swap for better image(s) – subfigure environment, correct coordinates.**

## 4.2 Circle and Lines Fit

Another way to estimate the particle’s kinetic energy is to fit its trajectory with a circular arc with lines attached smoothly. This shape of trajectory corresponds to a movement of a charged particle through a homogeneous magnetic field perpendicular to the particle’s momentum and limited to a certain volume. In general, the shape of such a trajectory in a non-perpendicularly oriented field is a spiral. In our case, this component is negligible since the field is approximately toroidal and the particle motion is nearly perpendicular to it. At first, we tested a 2D version of this fit, then we adapted it to 3D.

Our field is not homogeneous, it is therefore not entirely clear what value of magnetic field should be used along with the fitted radius (using equations 4.7 and 4.8) to get the best estimate for the kinetic energy. Since we only use this method as the first iteration of the particle’s energy that we later refine, an optimal solution of this problem is not required. Instead, we tested two options: taking the value of the field in the middle of the fitted circular arc and taking the average field along it. **We haven’t really tried to plot this for multiple tracks, but these estimates are saved somewhere and could be plotted.**

### 4.2.1 Two-dimensional fit

In the 2D case, the fitted function used for the electron track<sup>2</sup> described in Section 4.1 is defined as follows: **Maybe describe this track that we used at the beginning somewhere earlier (section microscopic simulations → Testing track?) so that it is easier to refer to it in multiple sections. It is not part of the early GitHub**

<sup>2</sup>Electron tracks bend towards negative  $z$ , we need to use the upper part of the circle

commits, so maybe it won't be possible to create exact replicas of the images, but they should be at least very similar.

$$z(x) = \begin{cases} a_1x + b_1 & x < x_1 \\ z_0 + \sqrt{r^2 - (x - x_0)^2} & x_1 \leq x \leq x_2, \\ a_2x + b_2 & x > x_2 \end{cases} \quad (4.9)$$

where  $a_{1,2}$  and  $b_{1,2}$  are the parameters of the lines,  $(x_0, z_0)$  is the center of the circle,  $r$  is its radius, and  $(x_{1,2}, z_{1,2})$  are the coordinates of the function's nodes. That means we have 9 parameters ( $z_{1,2}$  are not used in the function) along with 2 continuity conditions and 2 smoothness conditions. For the fit, we use the coordinates of the nodes and the radius of the circle, which gives us 5 independent parameters (only the radius has to be larger than half of the distance between nodes). The continuity conditions (combined with the relations for  $z_{1,2}$ ) are as follows:

$$z_{1,2} = a_{1,2}x_{1,2} + b_{1,2} = z_0 - \sqrt{r^2 - (x_{1,2} - x_0)^2}. \quad (4.10)$$

The smoothness conditions are as follows:

$$a_{1,2} = \frac{x_0 - x_{1,2}}{\sqrt{r^2 - (x_{1,2} - x_0)^2}}. \quad (4.11)$$

Equation 4.10 gives us the values of  $b_{1,2}$

$$b_{1,2} = z_{1,2} - a_{1,2}x_{1,2}. \quad (4.12)$$

For the coordinates of the center of the circle, we can use the fact that the center has to lie on the axis of its chord. In other words, there is a value of a parameter  $t$  such that, using the parametric equation of the axis

$$\begin{pmatrix} x_0 \\ z_0 \end{pmatrix} = \begin{pmatrix} \frac{x_1+x_2}{2} \\ \frac{z_1+z_2}{2} \end{pmatrix} + t \begin{pmatrix} \frac{z_2-z_1}{2} \\ \frac{x_1-x_2}{2} \end{pmatrix}. \quad (4.13)$$

At the same time, the center has to be in a distance of  $r$  from the nodes:

$$(x_1 - x_0)^2 + (z_1 - z_0)^2 = r^2, \quad (4.14)$$

$$\left(\frac{x_1 - x_2}{2} + \frac{z_1 - z_2}{2}t\right)^2 + \left(\frac{z_1 - z_2}{2} + \frac{x_2 - x_1}{2}t\right)^2 = r^2, \quad (4.15)$$

$$\left(\left(\frac{x_2 - x_1}{2}\right)^2 + \left(\frac{z_2 - z_1}{2}\right)^2\right)t^2 + \left(\frac{x_2 - x_1}{2}\right)^2 + \left(\frac{z_2 - z_1}{2}\right)^2 - r^2 = 0. \quad (4.16)$$

Since our electron track bends towards negative  $z$  and  $x_2 > x_1$ , we only care about the solution with  $t > 0$

$$t = \sqrt{\frac{r^2}{\left(\frac{x_2-x_1}{2}\right)^2 + \left(\frac{z_2-z_1}{2}\right)^2} - 1}, \quad (4.17)$$

$$x_0 = \frac{x_1 + x_2}{2} + \frac{z_2 - z_1}{2} \sqrt{\frac{r^2}{\left(\frac{x_2-x_1}{2}\right)^2 + \left(\frac{z_2-z_1}{2}\right)^2} - 1}, \quad (4.18)$$

$$z_0 = \frac{z_1 + z_2}{2} - \frac{x_2 - x_1}{2} \sqrt{\frac{r^2}{\left(\frac{x_2-x_1}{2}\right)^2 + \left(\frac{z_2-z_1}{2}\right)^2} - 1}. \quad (4.19)$$

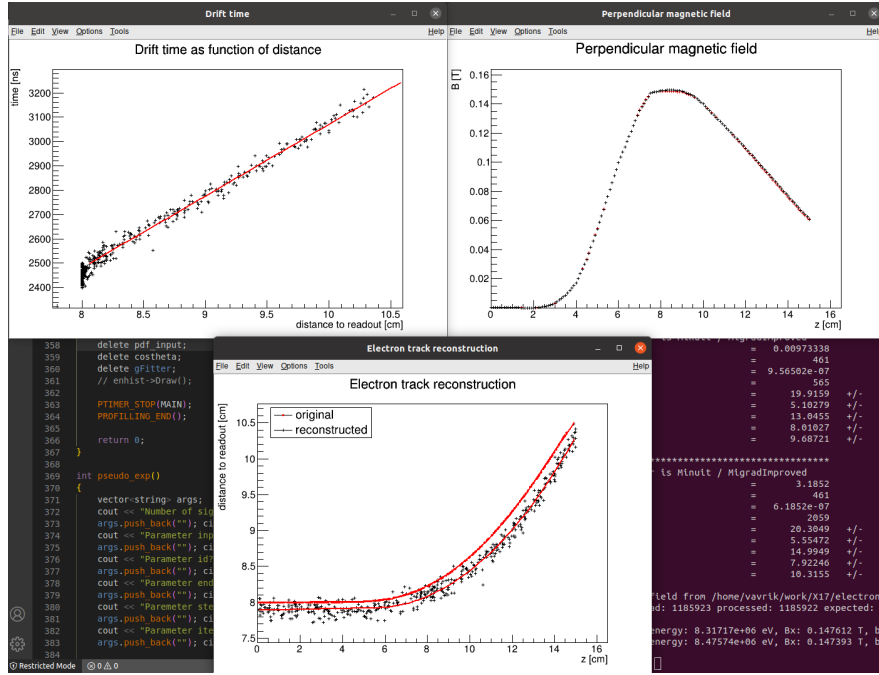


Figure 4.3: First attempt at a track reconstruction using only the drift velocity. Circle and Lines Fit in 2D. Swap for better image, correct coordinates.

571 The function defined in Equation 4.9 along with equations 4.11, 4.12, 4.18 and 4.19  
 572 derived using the continuity and smoothness conditions (combined with the re-  
 573 lations for  $z_{1,2}$ ) fully define our fitted function with parameters  $r, x_{1,2}, z_{1,2}$ . Some  
 574 pictures of the fit on the tested track. Results of the fit. Again, the actual fit  
 575 uses 8-z. Use GeoGebra schematics to generate a picture of 2D geometry.

576 Tested on a Runge-Kutta sample, and with microscopic tracks + map sim-  
 577 ulation. Preliminary 2D version (done) and complete 3D version. Geometry of  
 578 the fit with its derivation.

## 579 4.2.2 Three-dimensional fit

580 Explain the geometry and least square method used for the 3D fit.

## 581 4.3 Runge-Kutta Fit

582 Single parameter fit with 4th order Runge-Kutta simulated track. Future testing  
 583 with microscopic simulations and map simulation. Derivation of the geometry  
 584 (least squares).

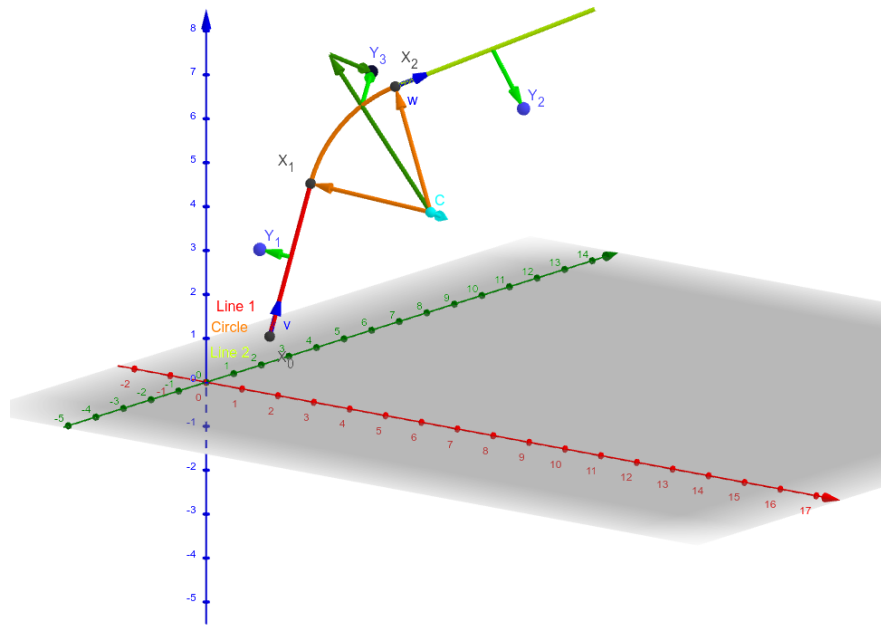


Figure 4.4: Circle and Lines Fit 3D geometry. [Swap for better image.](#)

# Conclusion

Here or at the end of each section. Something about the future of this work?

## Notes

General notes about the thesis:

- Check that all of the classes and other code are marked the same way in the text. I used italics somewhere, could use different font for this instead.
- Check unbreakable space in front of articles. Remove excessive article usage with proper nouns.
- Currently using margins for single-sided printing (bigger on the left side).
- Check that present tense is used
- American English quotation marks (") instead of British English (').
- Some of the overfull hbox warnings might change if duplex printing is used (they generate black rectangles on the edge of the page), leaving them be for now
- Check nobreakdash usage
- Check capitalized references (e.g., Figure, Section, Equation)
- Check  $\langle \dots \rangle$  math mode instead of  $\$ \dots \$$ . (actually unlike  $\langle \dots \rangle$  math mode, there is apparently no real benefit to this clumsy syntax)
- Use siunitx package to ensure correct formatting.
- Check other stuff that's written in the MFF UK template.

Random notes:

- Only electrons that start and end in the sector closer than 0.5 cm are used for reconstruction (newest version).

## Future

Things planned for the future:

- Testing the reconstruction algorithm by measuring real particles with a known energy distribution.
- The **Fast Simulation with Ionization Electron Map** is planned for the future. It will use the HEED program [24] to simulate the primary particle and the Ionization Electron Map (see Section 3.2) to simulate the drift of secondary electrons. It should be significantly faster than the Microscopic Simulation but offer comparable precision since it will rely on an already simulated drift map. (Primary track simulated in HEED. Readout parameters by interpolating the map. Diffusion from the map for randomization.)



- Account for GEM, delta electrons, ...
- Likelihood approach instead of least squares (if it improves the reconstruction significantly), we should at least use a better method than taking the center of the TPC bin.
- More detailed electric field simulation (if needed, GEM will have more complex field)

## Likelihood - inverse map

If we wanted to further improve this procedure, taking into account the whole map  $\mathcal{M}$ , we could make an "inverse map" from  $\mathcal{R}$  to distributions on  $\mathcal{D}$ . We could achieve this by taking the normalized probability density of an electron with initial coordinates  $(x, y, z)$  having readout coordinates  $(x', y', t)$ . If we fix  $(x', y', t)$ , we get an unnormalized probability density  $f(x, y, z) = \mathcal{M}_{(x, y, z)}(x', y', t)$  (assuming that all initial coordinates are a priori equally likely). This could potentially improve the discrete reconstruction if we take the mean value of this probability density across the pad and time bin

$$f_{\text{pad, bin}}(x, y, z) = \frac{1}{A_{\text{pad}} \Delta t_{\text{bin}}} \int_{\text{pad, bin}} \mathcal{M}_{(x, y, z)}(x', y', t) dx' dy' dt \quad (4.20)$$

and using it for a likelihood fit instead of using least squares. This still assumes that all initial coordinates are equally likely which is clearly not the case for a primary particle track. In the future, we could even use the fast track simulation with the map (should be possible to make around 1000 tracks per minute per core with current settings), create a big set of tracks with reasonable parameters and use these to get an approximation of the probability distribution of the detector response. Some approximations would be necessary when interpreting the data to decrease the degrees of freedom of this distribution (we would have to pick a set of parameters and assume that some of them are independent). This could give us an idea about the best achievable resolution (how significantly will the detector response differ for a given change in energy). If the difference is significant, we could try to further improve the likelihood fit.

# Bibliography

- [1] Garfield++. <https://garfieldpp.web.cern.ch/garfieldpp/>. Accessed: 2023-05-18.
- [2] Rene Brun and Fons Rademakers. Root — An Object Oriented Data Analysis Framework. *Nuclear Instruments and Methods in Physics Research Section A: Accelerators, Spectrometers, Detectors and Associated Equipment*, 389(1–2):81–86, Apr 1997. Proceedings AIHENP’96 Workshop, Lausanne, Sep. 1996, See also <https://root.cern/>, Paper published in the Linux Journal, Issue 51, July 1998.
- [3] About MetaCentrum. <https://metavo.metacentrum.cz/en/about/index.html>, 2023. Accessed: 2024-11-27.
- [4] M. E. Rose. Internal Pair Formation. *Phys. Rev.*, 76:678–681, Sep 1949.
- [5] R. Essig, J. A. Jaros, W. Wester, P. Hansson Adrian, S. Andreas, T. Averett, O. Baker, B. Batell, M. Battaglieri, J. Beacham, T. Beranek, J. D. Bjorken, F. Bossi, J. R. Boyce, G. D. Cates, A. Celentano, A. S. Chou, R. Cowan, F. Curciarello, H. Davoudiasl, P. deNiverville, R. De Vita, A. Denig, R. Dharmapalan, B. Dongwi, B. Döbrich, B. Echenard, D. Espriu, S. Fegan, P. Fisher, G. B. Franklin, A. Gasparian, Y. Gershtein, M. Graham, P. W. Graham, A. Haas, A. Hatzikoutelis, M. Holtrop, I. Irastorza, E. Izaguirre, J. Jaeckel, Y. Kahn, N. Kalantarians, M. Kohl, G. Krnjaic, V. Kubarovsky, H-S. Lee, A. Lindner, A. Lobanov, W. J. Marciano, D. J. E. Marsh, T. Maruyama, D. McKeen, H. Merkel, K. Moffeit, P. Monaghan, G. Mueller, T. K. Nelson, G. R. Neil, M. Oriunno, Z. Pavlovic, S. K. Phillips, M. J. Pivovarov, R. Poltis, M. Pospelov, S. Rajendran, J. Redondo, A. Ringwald, A. Ritz, J. Ruz, K. Saenboonruang, P. Schuster, M. Shinn, T. R. Slatyer, J. H. Steffen, S. Stepanyan, D. B. Tanner, J. Thaler, M. E. Tobar, N. Toro, A. Upadye, R. Van de Water, B. Vlahovic, J. K. Vogel, D. Walker, A. Weltman, B. Wojtsekhowski, S. Zhang, and K. Zioutas. Dark Sectors and New, Light, Weakly-Coupled Particles, 2013.
- [6] F.W.N. de Boer, O. Fröhlich, K.E. Stiebing, K. Bethge, H. Bokemeyer, A. Balanda, A. Buda, R. van Dantzig, Th.W. Elze, H. Folger, J. van Klinken, K.A. Müller, K. Stelzer, P. Thee, and M. Waldschmidt. A deviation in internal pair conversion. *Physics Letters B*, 388(2):235–240, 1996.
- [7] F W N de Boer, R van Dantzig, J van Klinken, K Bethge, H Bokemeyer, A Buda, K A Müller, and K E Stiebing. Excess in nuclear pairs near 9 MeV/ invariant mass. *Journal of Physics G: Nuclear and Particle Physics*, 23(11):L85, nov 1997.
- [8] F W N de Boer, K Bethge, H Bokemeyer, R van Dantzig, J van Klinken, V Mironov, K A Müller, and K E Stiebing. Further search for a neutral boson with a mass around 9 MeV/c<sup>2</sup>. *Journal of Physics G: Nuclear and Particle Physics*, 27(4):L29, apr 2001.

- [9] Attila Vitéz, A. Krasznahorkay, J. Gulyas, Margit Csátlos, Lorant Csige, Zoltan Gacsi, Barna Nyakó, F. Boer, T. Ketel, and J. Klinken. Anomalous Internal Pair Creation in  $^8\text{Be}$  as a Signature of the Decay of a New Particle. *Acta Physica Polonica B - ACTA PHYS POL B*, 39:483, 02 2008.
- [10] A. Krasznahorkay, J. Gulyas, Margit Csátlos, Attila Vitéz, T. Tornyai, L. Stuhl, Lorant Csige, Zoltan Gacsi, A. J. Krasznahorkay, M. Hunyadi, and T.J. Ketel. Searching for a light neutral axial-vector boson in isoscalar nuclear transitions. *Frascati Physics Series*, 56:86, 10 2012.
- [11] A. J. Krasznahorkay, M. Csatlós, L. Csige, Z. Gácsi, J. Gulyás, M. Hunyadi, I. Kuti, B. M. Nyakó, L. Stuhl, J. Timár, T. G. Tornyai, Zs. Vajta, T. J. Ketel, and A. Krasznahorkay. Observation of Anomalous Internal Pair Creation in  $^8\text{Be}$ : A Possible Indication of a Light, Neutral Boson. *Physical Review Letters*, 116(4), January 2016.
- [12] D.R. Tilley, J.H. Kelley, J.L. Godwin, D.J. Millener, J.E. Purcell, C.G. Sheu, and H.R. Weller. Energy levels of light nuclei  $A=8,9,10$ . *Nuclear Physics A*, 745(3):155–362, 2004.
- [13] N. J. Sas, A. J. Krasznahorkay, M. Csatlós, J. Gulyás, B. Kertész, A. Krasznahorkay, J. Molnár, I. Rajta, J. Timár, I. Vajda, and M. N. Harakeh. Observation of the X17 anomaly in the  $^7\text{Li}(p,e^+e^-)^8\text{Be}$  direct proton-capture reaction, 2022.
- [14] A. J. Krasznahorkay, M. Csatlós, L. Csige, J. Gulyás, A. Krasznahorkay, B. M. Nyakó, I. Rajta, J. Timár, I. Vajda, and N. J. Sas. New anomaly observed in  $^4\text{He}$  supports the existence of the hypothetical X17 particle. *Physical Review C*, 104(4), October 2021.
- [15] D.R. Tilley, H.R. Weller, and G.M. Hale. Energy levels of light nuclei  $A = 4$ . *Nuclear Physics A*, 541(1):1–104, 1992.
- [16] A. J. Krasznahorkay, A. Krasznahorkay, M. Begala, M. Csatlós, L. Csige, J. Gulyás, A. Krakó, J. Timár, I. Rajta, I. Vajda, and N. J. Sas. New anomaly observed in  $^{12}\text{C}$  supports the existence and the vector character of the hypothetical X17 boson. *Phys. Rev. C*, 106:L061601, Dec 2022.
- [17] F. Ajzenberg-Selove. Energy levels of light nuclei  $A = 11,12$ . *Nuclear Physics A*, 506(1):1–158, 1990.
- [18] Péter Kálmán and Tamás Keszthelyi. Anomalous internal pair creation. *The European Physical Journal A*, 56, 08 2020.
- [19] A. Aleksejevs, S. Barkanova, Yu. G. Kolomensky, and B. Sheff. A Standard Model Explanation for the "ATOMKI Anomaly", 2021.
- [20] Jonathan L. Feng, Bartosz Fornal, Iftah Galon, Susan Gardner, Jordan Smolinsky, Tim M. P. Tait, and Philip Tanedo. Protophobic Fifth-Force Interpretation of the Observed Anomaly in  $^8\text{Be}$  Nuclear Transitions. *Phys. Rev. Lett.*, 117:071803, Aug 2016.

- [21] Tran The Anh, Tran Dinh Trong, Attila J. Krasznahorkay, Attila Krasznahorkay, József Molnár, Zoltán Pintye, Nguyen Ai Viet, Nguyen The Nghia, Do Thi Khanh Linh, Bui Thi Hoa, Le Xuan Chung, and Nguyen Tuan Anh. Checking the 8Be Anomaly with a Two-Arm Electron Positron Pair Spectrometer. *Universe*, 10(4):168, April 2024.
- [22] Kh. U. Abraamyan, Ch. Austin, M. I. Baznat, K. K. Gudima, M. A. Kozhin, S. G. Reznikov, and A. S. Sorin. Observation of structures at  $\sim 17$  and  $\sim 38$  MeV/c<sup>2</sup> in the  $\gamma\gamma$  invariant mass spectra in pC, dC, and dCu collisions at  $p_{lab}$  of a few GeV/c per nucleon, 2023.
- [23] The MEG II collaboration, K. Afanaciev, A. M. Baldini, S. Ban, H. Benmansour, G. Boca, P. W. Cattaneo, G. Cavoto, F. Cei, M. Chiappini, A. Corvaglia, G. Dal Maso, A. De Bari, M. De Gerone, L. Ferrari Barusso, M. Francesconi, L. Galli, G. Gallucci, F. Gatti, L. Gerritzen, F. Grancagnolo, E. G. Grandoni, M. Grassi, D. N. Grigoriev, M. Hildebrandt, F. Ignatov, F. Ikeda, T. Iwamoto, S. Karpov, P. R. Kettle, N. Khomutov, A. Kolesnikov, N. Kravchuk, V. Krylov, N. Kuchinskiy, F. Leonetti, W. Li, V. Malyshev, A. Matsushita, M. Meucci, S. Mihara, W. Molzon, T. Mori, D. Nicolò, H. Nishiguchi, A. Ochi, W. Ootani, A. Oya, D. Palo, M. Panareo, A. Papa, V. Pettinacci, A. Popov, F. Renga, S. Ritt, M. Rossella, A. Rozhdestvensky. S. Scarpellini, P. Schwendimann, G. Signorelli, M. Takahashi, Y. Uchiyama, A. Venturini, B. Vitali, C. Voena, K. Yamamoto, R. Yokota, and T. Yonemoto. Search for the X17 particle in  ${}^7\text{Li}(p, e^+e^-){}^8\text{Be}$  processes with the MEG II detector, 2024.
- [24] I.B. Smirnov. Modeling of ionization produced by fast charged particles in gases. *Nuclear Instruments and Methods in Physics Research Section A: Accelerators, Spectrometers, Detectors and Associated Equipment*, 554(1):474–493, 2005.
- Acknowledgments:** Computational resources were provided by the e-INFRA CZ project (ID:90254), supported by the Ministry of Education, Youth and Sports of the Czech Republic.

# List of Figures

757			
758	1	The ATOMKI anomalous IPC measured for different nuclei. . . .	5
759	2	Results from the Hanoi spectrometer – angular $e^+e^-$ pair correlations measured in the ${}^7\text{Li}(p, e^+e^-){}^8\text{Be}$ reaction at $E_p = 1225$ keV [21].	6
760			
761	1.1	Pad layout of the TPC. <i>Swap for better image.</i> . . . . .	8
762	1.2	Visualization of trilinear interpolation as a composition of linear interpolations. <i>Image drawn in GeoGebra and inspired by a similar image on Wikipedia (which looks a bit worse) – is credit necessary?</i>	10
763			
764			
765	2.1	Example of a simulated electron track in 70 % argon and 30 % CO <sub>2</sub> atmosphere (on the left). <i>Swap for better images, better zoom. Explain drift lines, primary particle.</i> . . . . .	12
766			
767			
768	2.2	Comparison of diffusion in a simulated electron track in 70 % argon, 30 % CO <sub>2</sub> atmosphere and in 90 % argon, 10 % CO <sub>2</sub> atmosphere (on the right). <i>Swap for better image, better zoom. Or put the same pictures for both comparisons in one subfigure, etc. Describe better.</i> . . . . .	12
769			
770			
771			
772			
773	3.1	Dependence of the drift time on the $z$ coordinate in 90 % argon and 10 % CO <sub>2</sub> atmosphere, fitted with a linear function. The fitted function gives us the average drift velocity in the gas and can be used for rough reconstruction in our TPC. <i>Swap for better image with axis labels, etc. Maybe write the fitted equation.</i> . . . . .	14
774			
775			
776			
777			
778	3.2	First attempt at a track reconstruction using only the drift velocity. This approach works well in a standard TPC ( <i>ideally cite some source?</i> ). 90 % argon and 10 % CO <sub>2</sub> atmosphere. <i>Swap for better image, correct coordinates.</i> . . . . .	15
779			
780			
781			
782	3.3	First attempt at a track reconstruction using only the drift velocity, residues. <i>Swap for better image, correct coordinates. What's causing the shift? Explain details.</i> . . . . .	15
783			
784			
785	3.4	Example of map generation. <i>Swap for better image, correct coordinates.</i> . . . . .	17
786			
787	3.5	Example reconstruction with the map. <i>Swap for better image, correct coordinates.</i> . . . . .	18
788			
789	3.6	Selection of the points for interpolation. <i>Create better images; use the explanation interpolation vs. extrapolation strange property. Solution 2 probably does not make much sense.</i> . . . . .	20
790			
791			
792	4.1	Example of a fitted reconstructed track. <i>Swap for better image.</i> .	22
793	4.2	First attempt at a track reconstruction using only the drift velocity. Spline energy reconstruction attempt. <i>Swap for better image(s) – subfigure environment, correct coordinates.</i> . . . . .	24
794			
795			
796	4.3	First attempt at a track reconstruction using only the drift velocity. Circle and Lines Fit in 2D. <i>Swap for better image, correct coordinates.</i> . . . . .	26
797			
798			
799	4.4	Circle and Lines Fit 3D geometry. <i>Swap for better image.</i> . . . . .	27

# 800 List of Tables

# 801 List of Abbreviations

802 **HEED** High Energy Electro-Dynamics

803 **IEAP CTU** Institute of Experimental and Applied Physics, Czech Technical  
804 University in Prague

805 **IPC** Internal Pair Creation

806 **EPC** External Pair Creation

807 **MWPC** Multi-Wire Proportional Chamber

808 **OFTPC** Orthogonal Fields TPC

809 **TPC** Time Projection Chamber

810 **Tpx3** Timepix 3